Examination of the Br + HI, Cl + HI, and F + HI hydrogen abstraction reactions by photoelectron spectroscopy of $BrHI^-$, $ClHI^-$, and FHI^-

S. E. Bradforth,[a] A. Weaver,[b] D. W. Arnold,[c] R. B. Metz,[a] and D. M. Neumark[d]
Department of Chemistry, University of California, Berkeley, California, 94720

(Received 2 January 1990; accepted 9 May 1990)

The photoelectron spectra of the ions $BrHI^-$, $ClHI^-$, and FHI^-, along with their deuterated counterparts, are presented. These spectra provide information on the transition state region of the potential energy surfaces describing the exothermic neutral reactions $X + HI \rightarrow HX + I (X = Br, Cl, F)$. Vibrational structure is observed in the $BrHI^-$ and $ClHI^-$ spectra that corresponds to hydrogen atom motion in the dissociating neutral complex. Transitions to electronically excited potential energy surfaces that correlate to $HX + I(^2P_{3/2}, ^2P_{1/2})$ products are also observed. A one-dimensional analysis is used to understand the appearance of each spectrum. The $BrHI^-$ spectrum is compared to a two-dimensional simulation performed using time-dependent wave packet propagation on a model Br + HI potential energy surface.

I. INTRODUCTION

We have recently shown that negative ion photodetachment can be used to investigate the transition state region of a neutral bimolecular reaction.[1-3] In our experiments, the spectroscopy and dissociation dynamics of the short-lived [AHB] complex formed during the hydrogen transfer reaction $A + HB \rightarrow HA + B$ are studied via photoelectron spectroscopy of the stable, hydrogen-bonded anion AHB^-. Thus far, results have been reported for the symmetric hydrogen transfer reactions $Cl + HCl$,[1] $I + HI$,[2] and $Br + HBr$[3] which were investigated by photodetaching the negative ions $ClHCl^-$, IHI^-, and $BrHBr^-$, respectively. The photoelectron spectra of these ions show resolved vibrational progressions assigned to the unstable neutral complex associated with the corresponding bimolecular reaction. Our analysis as well as simulations of these spectra by other investigators[4-6] has shown that this vibrational structure provides a sensitive probe of the neutral potential energy surface near the transition state.

This paper describes the application of our method to asymmetric hydrogen transfer reactions. We have studied the entire series of reactions $X + HY \rightarrow HX + Y$, where X and Y are dissimilar halogen atoms, via photoelectron spectroscopy of the asymmetric bihalide ions XHY^-. In the same fashion, we have also conducted experiments on the polyatomic reactions $F + CH_3OH \rightarrow HF + CH_3O$ and $F + C_2H_5OH \rightarrow HF + C_2H_5O$.[7] Results are presented here for the triatomic reactions $Br + HI \rightarrow HBr + I$, $Cl + HI \rightarrow HCl + I$, and $F + HI \rightarrow HF + I$. The remaining XHY^- spectra and the $ROHF^-$ results will be discussed in a future article. In each case, the photoelectron spectrum of the precursor negative ion yields resolved vibrational and/or electronic structure associated with the unstable neutral complex formed by photodetachment.

In contrast to the symmetric hydrogen transfer reactions, a vast body of experimental results exists concerning the kinetics and product state distributions for the asymmetric reactions.[8] Experimental studies of the triatomic $X + HY$ reactions date back to the dawn of chemical reaction dynamics. This work has inspired the construction of model potential energy surfaces for these reactions which attempt to reproduce and explain the experimental results, using either classical trajectory[9,10] or quantum scattering[11] calculations. These model surfaces have provided the foundation of many fundamental ideas in our understanding of the relationship between the features of a potential energy surface and the experimentally measurable asymptotic properties of a chemical reaction. Our experiment provides a direct test of the validity of these proposed model $X + HY$ surfaces. Using such a surface, one can, in principle, simulate the XHY^- photoelectron spectrum and compare the simulation to our experimental result.

The methods of analysis which have been developed to simulate the vibrational structure seen in the XHX^- photoelectron spectra[3-6] can also be applied to the XHY^- photoelectron spectra. These methods all involve calculating the Franck–Condon overlap between the initial vibrational level of the ion and the set of scattering wave functions supported by the neutral potential energy surface. A one-dimensional analysis, in which the scattering coordinate is ignored, can approximately predict the spacing and integrated intensities of the peaks in each vibrational progression. This type of analysis is applied to the spectra presented in this paper as a first step in understanding our results.

In addition to probing the ground electronic potential energy surfaces of the $X + HY$ reactions, photodetachment of XHY^- anions can access electronically excited reactive surfaces. These excited states of the neutral complex are in most cases quite distinct in the spectra presented here and provide information on an aspect of these reactions largely

[a] University Fellow, University of California.
[b] NSERC (Canada) Postgraduate Scholar.
[c] NSF Predoctoral Fellow.
[d] NSF Presidential Young Investigator and Alfred P. Sloan Fellow.

 0021-9606/90/127205-18$03.00

inaccessible to scattering-based experiments. The electronic features in our spectra provide a more quantitative foundation for the electronic correlation diagrams proposed for these reactions[12,13] and are discussed at length.

Finally, the $BrHI^-$ photoelectron spectrum is simulated using time-dependent wave packet propagation in two dimensions. This approach simulates peak profiles and widths as well as peak separations, thus testing more stringently the accuracy of the potential surface used in this simulation, but differs from the time-independent treatments mentioned above in that the scattering wave functions are never calculated. The use and implementation of a time dependent formalism to describe spectral profiles due to a repulsive state draws on the ideas of Heller[14] and Kosloff.[15] The time-dependent approach provides considerable insight into the experimental results and makes more concrete the relationship between our experimental spectra and the short time dynamics initiated on the neutral reaction surface.

The systems chosen here illustrate both the promise and limitations of negative ion photodetachment as a probe of the neutral transition state region. The main concern is that the ion geometry must be similar to that of the neutral transition state. For symmetric X + HX reactions, the precursor ion XHX^- is most likely linear and centrosymmetric[16,17]; the only issue is how close the equilibrium interhalogen distance in the ion is to the saddle point geometry on the neutral surface. For an asymmetric X + HY reaction, an additional factor is the location of the hydrogen atom in XHY^-. This is largely determined by the proton affinities of X^- and Y^-. In a related experiment, Brauman and co-workers observed substantial differences in the total photodetachment cross sections for the series of ions $ROHF^-$ depending on whether the F^- or RO^- proton affinity is higher.[18] If RO^- has the higher proton affinity, then photodetachment of the ion primarily accesses the F + ROH entrance valley on the neutral reactive surface, whereas if the proton affinity of F^- is higher, the ion is more accurately pictured as $(RO^-)HF$ and photodetachment accesses the RO + HF exit valley of the surface. We shall see that these considerations have a profound effect on our experiment.

II. EXPERIMENTAL

The experiments were performed on a negative ion time-of-flight photoelectron spectrometer which has been described in detail previously.[3,19] Briefly, an internally cold, mass-selected negative ion beam is photodetached with a pulsed fixed-frequency laser. A small fraction of the ejected photoelectrons is collected and the electron kinetic energy distribution is analyzed by time of flight. The ion beam, based on the design of Lineberger and co-workers,[20] is generated by expanding an appropriate mixture of neutral gases through a pulsed molecular beam valve and crossing the molecular beam with a 1 keV electron beam just outside the valve orifice. Negative ions are formed through a variety of dissociative attachment and clustering processes in the continuum flow region of the free-jet expansion and their internal degrees of freedom are cooled as the expansion progresses. $BrHI^-$ and $ClHI^-$ were generated from a 5% HBr (HCl)/1% HI/Ar mixture and FHI^- was made from a 1% HF/1% HI/Ar mixture. Similar mixtures were used to make the ions $BrDI^-$, $ClDI^-$, and FDI^-.

Several centimeters downstream from the beam valve, the negative ions in the molecular beam are extracted at 90° and injected into a time-of-flight mass spectrometer.[21] The ions are accelerated to 1 keV and spatially separate into bunches according to their masses as they pass through the mass spectrometer. The pulsed photodetachment laser crosses the ion beam at the spatial focus of the mass spectrometer, 140 cm downstream from the extraction region. Mass selection of the ions to be photodetached is achieved by timing the laser pulse to intersect the ion bunch of the desired mass. In the results presented here, either the fourth (266 nm, 4.66 eV) or fifth harmonic (213 nm, 5.83 eV) of a Nd:YAG laser was used for photodetachment. A small fraction (0.01%) of the photoelectrons produced are detected by a 40 mm diameter dual microchannel plate detector 100 cm from the laser/ion beam interaction region. The electron time-of-flight distribution is recorded with a 200 MHz transient digitizer. In all experiments reported here, the laser beam was plane polarized perpendicular to the direction of electron collection. The resolution of the spectrometer is 8 meV for 0.65 eV electrons and degrades as $E^{3/2}$ at higher electron kinetic energies.

III. RESULTS

The $BrHI^-$ and $BrDI^-$ photoelectron spectra at 213 nm are shown in Fig. 1. Each spectrum shows two progres-

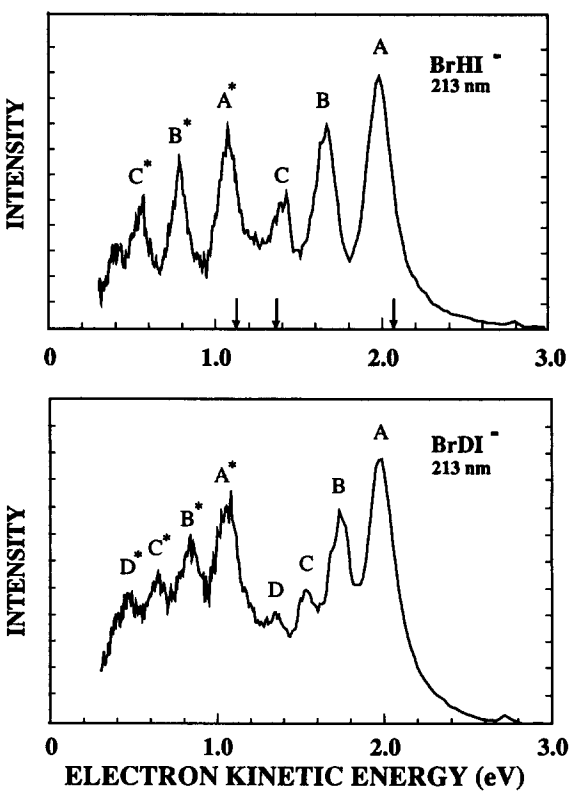

FIG. 1. The photoelectron spectra of $BrHI^-$ and $BrDI^-$ recorded at 213 nm. Arrows at 2.07, 1.36, and 1.12 eV represent asymptotes for dissociation into $I(^2P_{3/2}) + HBr(v=0)$, $Br(^2P_{3/2}) + HI(v=0)$, and $I(^2P_{1/2}) + HBr(v=0)$, respectively.

sions of approximately evenly spaced peaks. The peak positions are listed in Table I(a). The peaks labeled *A* and *A** occur at the same electron kinetic energy in both spectra and are taken to be band origins of the progressions. The peak spacing within each progression in Fig. 1 is noticeably less in the $BrDI^-$ spectrum than in the $BrHI^-$ spectrum. The direction of this isotope shift shows we are observing progressions in the neutral [BrHI] complex in a vibrational mode primarily involving H atom motion. This is assigned to the ν_3 stretching mode of the [BrHI] complex. The *A*–*A** separation in each spectrum is 0.90 ± 0.02 eV (7300 ± 200 cm^-). This is slightly less than the spin–orbit splitting in atomic I ($7600\ cm^{-1}$) and suggests that the two progressions with band origins *A* and *A** correspond to two electronic states of the [BrHI] complex which asymptotically correlate to $HBr + I(^2P_{3/2})$ and $HBr + I^*(^2P_{1/2})$, respectively.

The peak widths in the progression at higher electron kinetic energy are ~170 meV, somewhat wider than the peaks in the second progression (~140 meV). All the peaks are substantially broader than our experimental resolution. Figure 2, the photoelectron spectrum of $BrHI^-$ at 266 nm, shows only the first two peaks (*A* and *B*), where their electron kinetic energies are 1.165 eV lower than in Fig. 1. Thus, for these peaks, the energy resolution of the spectrometer is considerably higher (8 me V compared to 37 meV). While

TABLE I. Experimental results for photoelectron spectra of (a) $BrHI^-$ and $BrDI^-$, (b) $ClHI^-$ and $ClDI^-$, and (c) FHI^- and FDI^-. (All energies in eV.)

(a)	eKE[a] 213 nm	FWHM[b] 213 nm	eKE[a] 266 nm	FWHM[b] 266 nm	Spacing	Spacing in HBr/DBr[c]
$BrHI^-$						
A	1.970 (17)	0.175	0.783 (4)	0.170		
					0.313 (5)[d]	0.317 (0–1)
B	1.658 (13)	0.170	0.470 (3)	0.165		
					0.268 (18)	0.306 (1–2)
C	1.390 (10)	0.160				
*A**	1.071 (7)	0.155				
					0.292 (9)	0.317 (0–1)
*B**	0.779 (5)	0.140				
					0.234 (10)	0.306 (1–2)
*C**	0.545 (8)	~0.120				
A→*A** spacing is 0.899 ± 0.019 eV; iodine atom spin–orbit splitting is 0.943 eV						
$BrDI^-$						
A	1.980 (17)	0.185				
					0.240 (22)	0.228 (0–1)
B	1.740 (14)	0.170				
					0.203 (18)	0.222 (1–2)
C	1.537 (11)	0.160				
					0.193 (19)	0.216 (2–3)
D	1.344 (15)	~0.160				
*A**	1.068 (9)	0.180				
					0.226 (15)	0.228 (0–1)
*B**	0.842 (11)	0.170				
					0.192 (17)	0.222 (1–2)
*C**	0.650 (13)	~0.150				
					0.170 (20)	0.216 (2–3)
*D**	0.480 (15)	~0.170				
A→*A** spacing is 0.912 ± 0.020 eV						

(b)	eKE[a] 213 nm	FWHM[b] 213 nm	eKE[a,c] 266 nm	FWHM[b,c] 266 nm	Spacing	Spacing in HCl/DCl[c]
$ClHI^-$						
A	2.070 (17)	0.230	0.900 (5)	0.220		
					0.380 (6)[d]	0.358 (0–1)
B	1.678 (13)	0.220	0.520 (3)	0.220		
					0.323 (18)	0.345 (1–2)
C	1.355 (13)	~0.210				
*A**	1.133 (10)	0.185				
					0.358 (17)	0.358 (0–1)
*B**	0.775 (13)	~0.180				
A→*A** spacing is 0.937 ± 0.020 eV						

Table I (*continued*).

(b)	eKE[a] 213 nm	FWHM[b] 213 nm	eKE[a,c] 266 nm	FWHM[b,c] 266 nm	Spacing	Spacing in HCl/DCl[c]
$ClDI^-$						
A	2.079 (17)	0.205	0.900 (5)	0.190		
					0.279 (7)[d]	0.259 (0–1)
B	1.797 (14)	0.190	0.621 (4)	0.175		
					0.258 (19)	0.252 (1–2)
C	1.539 (13)	~0.175				
*A**	1.148 (8)	0.175				
					0.278 (14)	0.259 (0–1)
*B**	0.870 (11)	0.175				
					0.235 (17)	0.252 (1–2)
*C**	0.635 (13)	~0.170				

A→*A** spacing is 0.931 ± 0.019 eV

(c)	eKE[a] 213 nm	FWHM[b] 213 nm	eKE[a] 266 nm	FWHM[b] 266 nm	Spacing
FHI^-					
X	2.143 (19)	0.100			
					0.151 (25)
Y	1.992 (17)	0.130			
					0.894 (19)
Z	1.098 (7)	0.115			
FDI^-					
X	2.143 (19)	0.100	0.966 (5)	0.070	
					0.154 (7)[e]
Y	1.992 (17)	0.130	0.812 (4)	0.110	
					0.894 (19)
Z	1.098 (7)	0.115			

[a] Electron kinetic energies (eKE) at each peak center found by fitting peaks to a set of Gaussians. Uncertainties, in parentheses, are approximate.
[b] Uncertainties in widths are approximately 0.005 eV, except where indicated.
[c] Spacings between vibrational levels indicated in parentheses; source Ref. 39.
[d] *A–B* spacing from 266 nm data.
[e] 266 nm spectra not shown.
[f] *X–Y* spacings from 266 nm data.

the positions of these peak centers can be determined more precisely from Fig. 2, the appearance of this region of the spectrum is essentially unchanged from Fig. 1; no additional structure is observed at higher resolution. The 266 nm data are also tabulated in Table I(a).

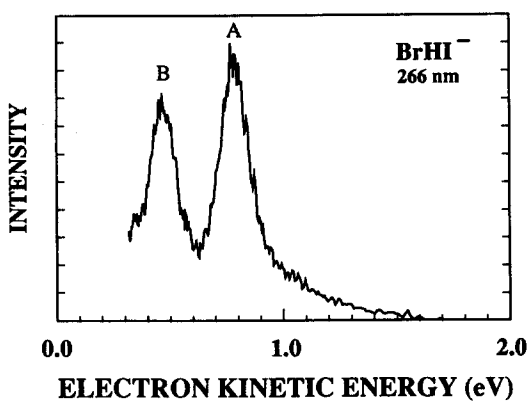

FIG. 2. The photoelectron spectrum of $BrHI^-$ recorded at 266 nm.

The exothermicity of the Br + HI reaction and relevant energetic quantities for the $BrHI^-$ anion are tabulated in Table II, as are the same quantities for the other systems studied here. In Fig. 1, the arrow at 2.07 eV shows the electron kinetic energy that would result from forming $I + HBr(v = 0)$, which is the lowest energy asymptotic decay channel available to the [BrHI] complex. This energy is given by $E = h\nu - D_0(BrHI^-) - EA(I)$. Here $h\nu$ is the photon energy, $D_0(BrHI^-) = 0.70 \pm 0.04$ eV is the dissociation energy of $BrHI^-$ to form $I^- + HBr(v = 0)$,[22] and $EA(I) = 3.059$ eV is the electron affinity of I.[23] The electron energy corresponding to the higher energy $Br + HI(v = 0)$ asymptote is also indicated with the arrow at 1.36 eV. All of the peaks in Fig. 1 occur at electron kinetic energies *lower* than 2.07 eV and therefore correspond to states of the [BrHI] complex that are *unstable* with respect to dissociation to $I + HBr(v = 0)$. Recall that peaks at lower electron kinetic energy correspond to higher internal energy levels of the neutral species.

As discussed in previous work,[3] the ν_3 mode in the complex formed in a heavy + light–heavy reaction is essentially

TABLE II. Available data for the anions and neutral reactions described in this work.

Anion	$BrHI^-$	$BrDI^-$	$ClHI^-$	$ClDI^-$	FHI^-	FDI^-
ΔH^0_{300} (eV)[a]	0.70		0.62		0.65[b]	
ν_3 (cm^{-1})[c]	920[d]	728[d]	1560[d]	1219[d]	2955[e]	2225[e]
E.B.E. (eV)[f]	3.88	3.85	3.76	3.76	3.68	3.70
Neutral reaction	Br + HI	Br + DI	Cl + HI	Cl + DI	F + HI	F + DI
ΔH^0_0 (eV)[g]	0.704	0.710	1.379	1.390	2.815	2.843

[a] Hydrogen bond cleavage enthalpy, i.e., the enthalpy change for the reaction $XH\cdots I^- \rightarrow XH + I^-$ at 300 K, from Ref. 22. This value is used, in the absence of other data, for $D_0(XH\cdots I^-)$ in the text.
[b] Estimated. See Ref. 24 for details.
[c] Fundamental frequency for the type I hydrogen stretching vibration, measured for ion prepared in an argon matrix. See text for discussion of choice of frequencies.
[d] Reference 29.
[e] Reference 30.
[f] Approximate electron binding energy. This is estimated from center of 0–0 peak in photoelectron spectrum (this work).
[g] Reaction exothermicity: $\Delta H^0_0 = D^0_0(HX) - D^0_0(HI)$. Data from Ref. 36.

a bound degree of freedom; it is poorly coupled to the dissociation coordinate of the complex. This is why a progression in the ν_3 mode can be observed in the $BrHI^-$ photoelectron spectrum. The ν_3 progressions and multiple electronic states in the $BrHI^-$ and $BrDI^-$ spectra were also seen in the symmetric XHX^- photoelectron spectra. An important difference between the symmetric and asymmetric systems becomes apparent, however, when the peak separations are compared to the asymptotic HBr and DBr vibrational energy level spacings [refer to Table I(a)]. In the $BrHBr^-$ spectrum, the peak separation was nearly 1000 cm^{-1} (0.13 eV) less than the HBr spacings. Much smaller shifts are seen in the $BrHI^-$ and $BrDI^-$ spectra. Table I(a) shows that for the ground state progressions of both [BrHI] and [BrDI], the separation between peaks A and B is essentially equal to the $v = 0 \rightarrow v = 1$ spacing in HBr and DBr. However, the B–C separation in both spectra, and the C–D separation for the $BrDI^-$ spectrum, are smaller than the corresponding 1–2 and 2–3 vibrational spacings in the isolated diatomic. In the excited state progressions, a somewhat larger shift of the ν_3 level spacing is observed.

The $ClHI^-$ and $ClDI^-$ spectra at 213 nm are shown in Fig. 3. A comparison of the two spectra indicates that each consists of two vibrational progressions separated by 0.935 ± 0.020 eV (7540 ± 160 cm^{-1}). As in the $BrHI^-$/$BrDI^-$ spectra, the two progressions are attributed to different electronic states of [ClHI], and once again all peaks correspond to states of the [ClHI] complex that are unstable with respect to dissociation into I + HCl($v = 0$).[22,23] The most noticeable difference between the spectra in Fig. 1. and Fig. 3 is that the intensity of transitions to higher ν_3 levels of the neutral complex fall of more rapidly in the $ClHI^-$ and $ClDI^-$ spectra than in $BrHI^-$/$BrDI^-$. The peak positions and widths are listed in Table I(b). In comparison to the $BrHI^-$ and $BrDI^-$ spectra the peak separations in $ClHI^-$ and $ClDI^-$ spectra are somewhat closer to the corresponding HCl and DCl vibrational spacings. In fact, the *A–B* interval is just slightly larger than the diatomic 0–1 interval in both hydride and deuteride.

The FHI^- and FDI^- spectra at 213 nm are shown in Fig. 4. The peak positions are listed in Table I(c). The two spectra are essentially identical. Each spectrum shows three

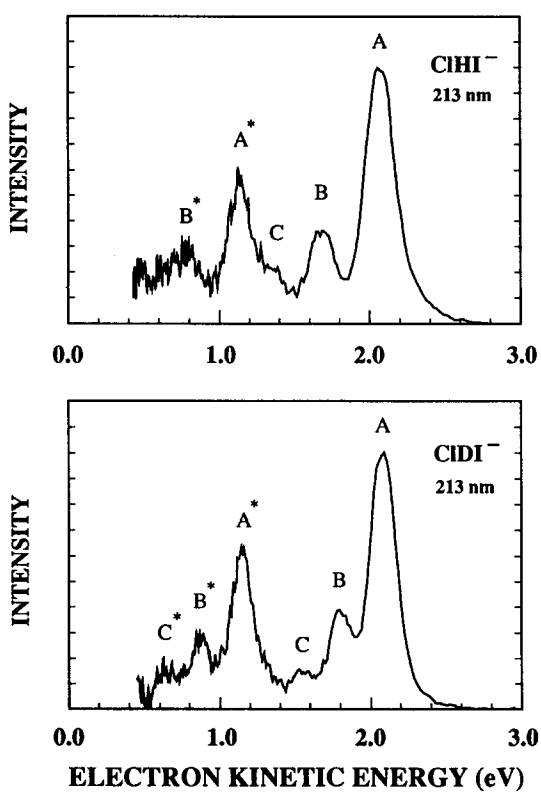

FIG. 3. The photoelectron spectra of $ClHI^-$ and $ClDI^-$ recorded at 213 nm.

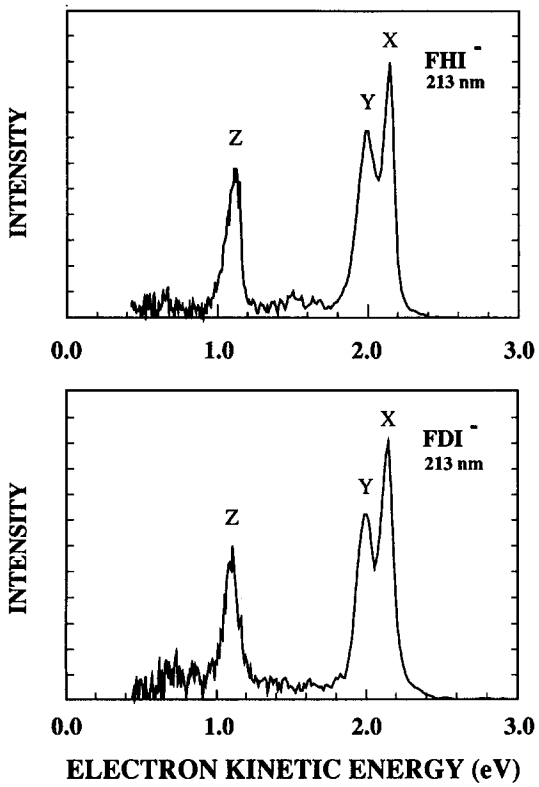

FIG. 4. The photoelectron spectra of FHI^- and FDI^- recorded at 213 nm.

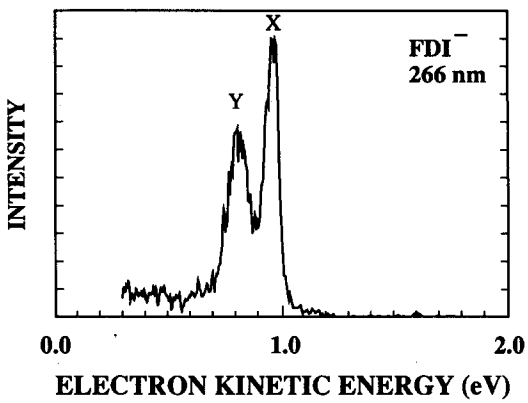

FIG. 5. The photoelectron spectrum of FDI^- recorded at 266 nm.

peaks of comparable intensity. The splitting between the two highest energy peaks (labeled X and Y) is shown to better resolution in Fig. 5, the photoelectron spectrum of FDI^- at 266 nm. This splitting is 0.154 ± 0.007 eV (1240 ± 60 cm^{-1}). The large uncertainty in the dissociation energy[24] of FHI^- does not allow us to say whether or not the state that corresponds to peak X is stable with respect to dissociation into $I + HF(v = 0)$ The separation between peaks X and Z is 1.045 ± 0.020 eV (8430 ± 160 cm^{-1}), which is larger than the separation between the two progressions in either the $BrHI^-$ or $ClHI^-$ spectrum. In contrast to the $BrHI^-/BrDI^-$ and $ClHI^-/ClDI^-$ spectra, no isotope shifts are observed. This implies that the two closely spaced peaks, X and Y, do *not* represent a vibrational progression and that all the structure in the spectrum is due to different electronic states of the [FHI] complex. We will show that this can be understood in terms of perturbations of the I atom electronic states by a neighboring HF molecule.

IV. ANALYSIS AND DISCUSSION

A. Preliminary considerations

As a prelude to understanding the peak positions and intensities in the XHY^- photoelectron spectra, one must consider what region of the X + HY potential energy surface is probed when the ion is photodetached. Within the framework of the Franck–Condon approximation, this depends solely on the geometry of the ion. The available experimental[16] and theoretical[17] evidence indicates that the bihalide ions are linear. However, while *ab initio* calculations on $FHCl^-$ have yielded both structural information[25] and vibrational frequencies,[26] there are no examples for which the equilibrium interhalogen distance and location of the hydrogen atom in an asymmetric XHY^- ion have been experimentally determined. One can estimate the location of the hydrogen atom in XHY^- from the proton affinities of X^- and Y^-. The zero-order structure of an asymmetric anion can be written as $XH\cdot\cdot Y^-$ or $X^-\cdot\cdot HY$ depending on whether the proton affinity of X^- or Y^- is higher. The proton affinities of F^-, Cl^-, and Br^- are 2.47, 0.82, and 0.40 eV higher, respectively, than the proton affinity of I^-.[27] One therefore expects $BrHI^-$ to look like $I^-\cdot\cdot HBr$, with the hydrogen atom considerably closer to the Br than to the I atom. This asymmetry should become progressively more pronounced in $ClHI^-$ and FHI^-.

To understand the effects of the interhalogen distance and H atom location in XHY^- on the photoelectron spectrum, the potential energy surface for the neutral reaction must be considered. Figure 6 shows[28] a collinear section of the London–Eyring–Polanyi–Sato (LEPS) functional form proposed for the Br + HI reaction by Broida and Persky (hereafter referred to as the BP surface).[10] The three-dimensional surface has a collinear minimum energy path and a 0.21 kcal/mol barrier in the Br + HI entrance valley. The surface is plotted using the mass-weighted coordinates defined in the figure caption. The acute skew angle and low entrance channel barrier in Fig. 6 are characteristic of all X + HY reactions.

The region of the surface in Fig. 6 that has the best Franck–Condon overlap with $BrHI^-$ is in the neighborhood of the equilibrium geometry of the ion. In the figure, this geometry is given by the intersection of the dashed vertical line corresponding to the equilibrium interhalogen distance in the ion [R_e(IBr)] and the dashed horizontal line corresponding to the location of the H atom [R_e(HBr)]. The values for R_e(IBr) and R_e(HBr) used in the figure are obtained from the one dimensional fit discussed in Sec. IV B. For the general X + HY case, if R_e(XY) is sufficiently small in XHY^-, the corresponding vertical line in Fig. 6 will pass through or near the barrier. Our experiment can then probe the transition state region on the X + HY surface, where the vibrational and/or electronic properties of the

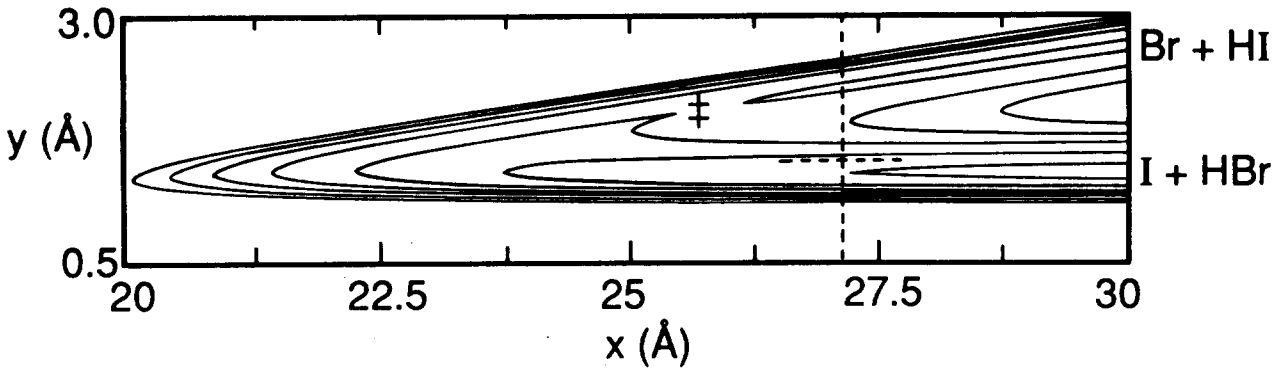

FIG. 6. The *effective collinear* LEPS surface for the Br + HI reaction, derived from that of Broida and Persky, plotted in mass-weighted coordinates defined by $x = (\mu_{I,HBr}/\mu_{HBr})^{1/2}[R_I - R_{cm}(HBr)] \approx (\mu_{I,HBr}/\mu_{HBr})^{1/2} R_{I\text{-}Br} \sim 7.0 R_{I\text{-}Br}$, $y = R_{H\text{-}Br}$. Here R_I and R_{cm} (HBr) are the position of the I atom and the HBr center-of-mass, respectively, and μ_{AB} signifies the reduced mass of system *A–B*. The skew angle θ is given by $\tan\theta = (m_H M/m_{Br} m_I)^{1/2}$ which for this system is 8.2°, noting that $M = m_I + m_H + m_{Br}$. Contours are plotted at 0.161, 0.461, 0.761, 1.061, 1.361, 1.661, and 1.961 eV with respect to the I + HBr asymptote. The assumed anion equilibrium geometry is marked by the intersection of the dashed vertical and horizontal lines, at $x_e = 27.11$ and $y_e = 1.55$ Å, and the saddle point is marked with ‡.

[XHY] complex are distinct from separated reactants or products. On the other hand, R_e(HX) in the ion determines whether photodetachment primarily accesses the X + HY reactant valley or the Y + HX product valley.

In the case of $BrHI^-$, since the ion can be pictured as $I^- \cdots HBr$, better overlap with the I + HBr product valley rather than the reactant valley is expected. The most intense peaks seen in the experimental spectrum lie well below the asymptote for Br + HI($v = 0$) confirming that the experiment accesses the product valley. However, the observation of a red shift in the ν_3 spacings of the [BrHI] and [BrDI] complexes, compared to the vibrational level spacings in HBr and DBr, suggests that R_e(IBr) in $BrHI^-$ is sufficiently small that the transition state region of the Br + HI surface is accessed via photodetachment.

Similar considerations apply to the $ClHI^-$ and FHI^- photoelectron spectra. The potential energy surfaces for the Cl + HI and F + HI reactions should resemble the surface in Fig. 6, although earlier barriers might be expected due to the higher exothermicity of these reactions. However, the expected location of the H atom in $ClHI^-$ and FHI^- means that photodetachment should result in progressively greater overlap with the I + HX product valley. This effect will be discussed in more detail below.

B. One-dimensional analysis of XHY^- spectra

In this section, the peak positions and intensities of the ground state vibrational progressions in the three XHY^- (and XDY^-) photoelectron spectra are analyzed using a one-dimensional model similar to that used in the analysis of the $BrHBr^-$ spectrum.[3] The $BrHI^-$ and $BrDI^-$ spectra are simulated using this model, which then serves as a framework for discussing the $ClHI^-$ and FHI^- spectra. In addition to explaining the observed spectra, the analysis yields an approximate equilibrium geometry for $BrHI^-$ which will be used in the time-dependent analysis in Sec. IV D.

1. $BrHI^-$ and $BrDI^-$

In order to simulate the peak positions and intensities in the $BrHI^-$ and $BrDI^-$ photoelectron spectra, we need to calculate the Franck–Condon overlap between the $v_3 = 0$ level of the ion and the v_3 levels supported by the neutral potential energy surface. We assume the ions prepared in our experiment are in their vibrational ground states. This analysis requires approximate potential energy surfaces for $BrHI^-$ and the Br + HI reaction. We will use the BP surface, shown in Fig. 6, for the Br + HI reaction. The development of a model ν_3 potential for $BrHI^-$ will now be discussed.

In our earlier analysis of the symmetric XHX^- spectra, we assumed a harmonic potential for the ν_3 vibration of the ion. This is likely to be a poor approximation for an asymmetric XHY^- ion. In an *ab initio* study on $FHCl^-$, Sannigrahi and Peyerimhoff[25] calculated the potential energy curves governing H atom motion for several fixed interhalogen distances. At the equilibrium F–Cl distance, they found a highly asymmetric, single minimum potential. Based on the $FHCl^-$ calculation, the analogous potential energy curve for $BrHI^-$ is expected to look like the solid curve in Fig. 7. For the purposes of calculating the $v_3 = 0$ wave function which is localized near the minimum, this curve can be approximated by the Morse potential,

$$U(R_{H\text{-}Br}) = D_e(1 - \exp\{-\beta[R_{H\text{-}Br} - R_e(HBr)]\})^2, \quad (1)$$

shown by the dashed curve in Fig. 7. We use Eq. (1) as the ν_3 stretching potential for $BrHI^-$. The ν_3 coordinate is $R_{H\text{-}Br}$, and μ_{HBr} is the appropriate reduced mass for determining the vibrational energy levels and wave functions. Here R_e(HBr) is the H–Br separation at the minimum of the potential; its determination is described below.

The parameters D_e and β in Eq. (1) are fixed using the matrix isolation values for the ν_3 fundamental in $BrHI^-$ and $BrDI^-$ (Ref. 29). The choice of these values merits some discussion. Matrix studies by Ault and co-workers

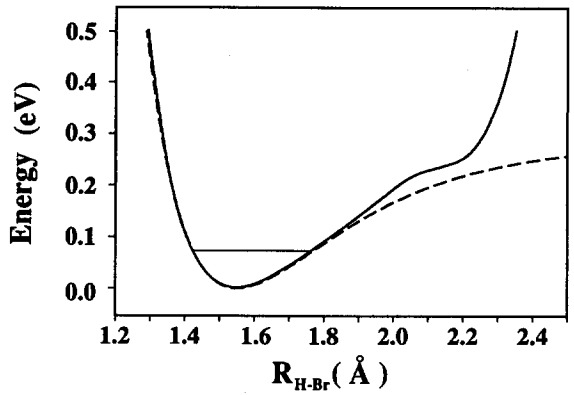

FIG. 7. Potential along hydrogen stretching coordinate (ν_3) in $BrHI^-$ anion: expected form (solid) based on *ab initio* potential for $FHCl^-$ (Ref. 25) and the Morse potential (dashed) used to model this. The lowest vibrational eigenstate of the model potential is also shown. Morse parameters are $D_e = 0.283$ eV and $\beta = 3.243$ Å^{-1}.

yielded two frequencies assignable to the ν_3 mode for each asymmetric XHY^- ion.[29,30] This was attributed to the existence of two forms of the ion in a matrix: a highly asymmetric structure (type I) with a relatively high ν_3 frequency, and a more symmetric structure (type II) with a considerably lower frequency. For $FHCl^-$, the ν_3 fundamental is 2491 cm^{-1} for the type I structure and 933 cm^{-1} for the type II structure.[30] The high degree of asymmetry in Peyerimhoff's potential[25] and a recently calculated value by Botschwina[26] of 2814 cm^{-1} for the ν_3 fundamental in $FHCl^-$ suggest that the more asymmetric type I structure is closer to the gas phase structure. We have therefore used the type I frequencies,[29] 920 and 728 cm^{-1}, for the ν_3 fundamental in $BrHI^-$ and $BrDI^-$, respectively. D_e and β are then obtained analytically.

The BP potential energy surface in Fig. 6 will be assumed for the Br + HI reaction. This surface was devised on the basis of quasi-classical trajectory calculations which produce reasonable agreement with the experimental rate constants at several temperatures and the product HBr $v = 2/v = 1$ ratio at 300 K.[10] The ν_3 coordinate is taken to be the same as in the ion, namely $y = R_{H\text{-}Br}$. Thus, the effective potential for the hydrogen stretch in the neutral [BrHI] complex is found by taking a vertical cut through the surface at $x = x_e$, the value of x at the equilibrium structure of the ion given by

$$x_e = (\mu_{I,HBr}/\mu_{HBr})^{1/2}[R_e(IBr) - (m_H/m_{HBr})R_e(HBr)]. \quad (2)$$

Note that $m_H/m_{HBr} \approx 1/80$, so to a good approximation $x_e \approx 7.0R_e(IBr)$. Here, as before, $R_e(IBr)$ is the equilibrium interhalogen distance in the ion. The energy levels and wave functions supported by this potential are then solved for numerically.

The peak spacings and intensities in the $BrHI^-$ photoelectron spectrum can now be simulated by calculating the Franck–Condon factors between the $v_3 = 0$ ion level supported by the Morse potential in Eq. (1) and the ν_3 levels supported in the neutral surface cut at $x = x_e$. We assume the BP surface is correct and vary $R_e(IBr)$ and $R_e(HBr)$ in the ion until agreement with experiment is obtained. $R_e(IBr)$ largely determines the location of the cut on the neutral surface which in turn determines the peak spacings in the photoelectron spectra. The value of $R_e(HBr)$ determines the position of the minimum in the Morse potential for the ion along the y axis of Fig. 6 and therefore determines the intensity distribution of the simulated spectra. The best fit to both the $BrHI^-$ and $BrDI^-$ spectra is obtained with $R_e(HBr) = 1.55$ Å and $x_e = 27.1$ Å, so $R_e(IBr) \approx 3.88$ Å. The hydrogen stretching ν_3 potentials for ion and neutral are shown in Fig. 8 along with the energies of the ion $v_3 = 0$ and 1 levels and the first few neutral ν_3 levels. The simulated stick spectra are superimposed on the experimental spectra in Fig. 9.

This one-dimensional analysis provides a firmer foundation for some of the qualitative ideas discussed in the previous section. Although the line $x = x_e$ in Fig. 6 passes very close to the barrier, the $v_3 = 0$ level of $BrHI^-$ has the most overlap with the $v_3 = 0$, 1 and 3 levels supported by the neutral potential. The wave functions for these levels are confined to the I + HBr product valley of the potential energy surface and can be thought of as HBr vibrational levels perturbed by a neighboring I atom. This is why the peaks in the spectrum corresponding to transitions to these states are spaced by an interval only slightly less than the HBr fundamental. Note that the $v_3 = 2$ wave function is localized in the Br + HI valley. The anion wavefunction has very little over-

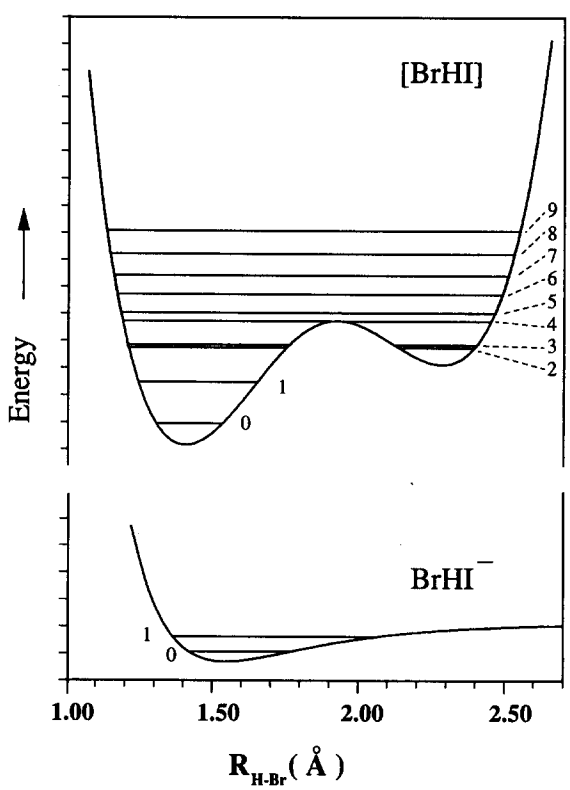

FIG. 8. Anion and neutral ν_3 potentials used in the one-dimensional analysis of $BrHI^-$ spectrum. Calculated eigenstates are labelled by their v_3 quantum number. Each tick mark on vertical axis represents 0.2 eV.

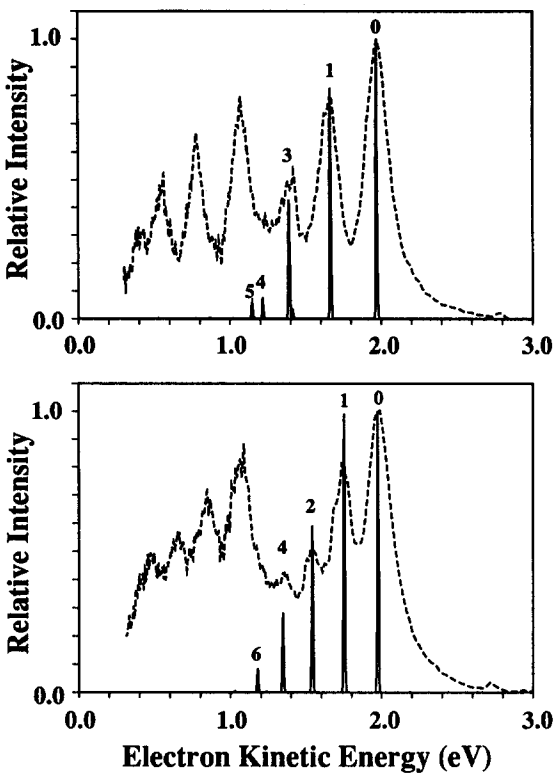

FIG. 9. Franck–Condon stick spectra for (top) $BrHI^-$ and (bottom) $BrDI^-$, simulated in one-dimensional time-independent analysis. Simulations superimposed on the respective experimental spectra (dashed). Simulated sticks are labeled by v_3 quantum numbers and for the $BrHI^-$ spectrum correspond to those shown on Fig. 8.

lap with this state but it does appear in the simulation as a small peak to the right of peak 3 in Fig. 9 (top).

2. $ClHI^-$ and FHI^-

The differences between the $ClHI^-$ and $BrHI^-$ photoelectron spectra can be understood by considering how the potential energy curves in Fig. 8 should differ in the case of $ClHI^-$ photodetachment. The product valley well in the neutral ν_3 potential should be deeper because the Cl + HI reaction is more exothermic (see Table II). Thus the first few ν_3 levels supported by this potential should look much like isolated HCl vibrational energy levels. This is confirmed by the peak spacings in Table I(b), which show little or no red shift relative to the HCl and DCl vibrational energy levels. In addition, because of the larger difference in proton affinities between the halide ions in $ClHI^-$ compared to $BrHI^-$, $ClHI^-$ will look more like I^- clustered to a nearly unperturbed HCl molecule. We therefore expect the minima in the ν_3 potentials for the anion and neutral to occur at a value of $R_{H\text{-}Cl}$ quite close to the equilibrium value for diatomic HCl; the two minima should be much closer than the minima in the two potentials in Fig. 8. Hence $\Delta v_3 = 0$ transitions to the neutral are expected to dominate more than in $BrHI^-$ photodetachment, in agreement with our observations.

The absence of a ν_3 progression in the FHI^- and FDI^- photoelectron spectra can also be explained by considering the ν_3 potentials for the ion and neutral. The F + HI reaction is considerably more exothermic than either the Br + HI or the Cl + HI reactions, and the ion should be even more asymmetric than either $BrHI^-$ or $ClHI^-$. Thus, we expect the ν_3 potentials for the anion and neutral complex to look very much like the diatomic HF potential, at least near the bottom of the wells. With reference to Fig. 8, in the case of FHI^- photodetachment we expect that the wells in the ion and neutral potentials are very similar in shape and their minima essentially coincide (at R_e for diatomic HF); this results in only $\Delta v_3 = 0$ transitions in the photoelectron spectrum.

C. Electronic structure in the XHY^- spectra

We now consider the electronic structure revealed in the XHY^- photoelectron spectra. Photodetachment of XHY^- provides a direct probe of the multiple electronic potential energy surfaces in the HX + Y product valley (in the present case where Y = I). This is of considerable interest in light of past work on the role of electronically excited reactant and product states in these reactions.[12,13,31–33]

Let us first consider which neutral electronic states are accessible via photodetachment of XHY^-, a closed shell $^1\Sigma^+$ species. Based on the simple molecular orbital picture proposed for FHF^- by Pimentel,[34] the two highest occupied molecular orbitals in XHY^- are expected to be a σ orbital which is a linear combination of the two halogen $2p_z$ and H $1s$ orbitals, and a doubly degenerate π orbital of the form $2p_{x,y}(X)$–λ $2p_{x,y}(Y)$. Removal of an electron from the σ orbital by photodetachment results in a neutral $^2\Sigma$ state, whereas removal of an electron from the π orbital yields a $^2\Pi$ state. If spin–orbit interactions are neglected in the collinear X + HY reaction, then when the ^2P X atom begins interacting with the HY molecule, the lowest energy electronic state should be the Σ state in which the unfilled p orbital on the X atom lies along the XHY internuclear axis. On the other hand, the Π state, in which the unfilled orbital lies perpendicular to this axis, should result in a repulsive interaction. This is confirmed by DIM (diatomics-in-molecules) calculations by Duggan and Grice for the related systems F + HF and Cl + HCl.[32]

The inclusion of spin–orbit interactions results in a slightly more complicated picture of the electronic states involved in the reaction. A correlation diagram for the Br + HI reaction including spin–orbit effects is shown in Fig. 10.[35] The figure can be generalized to all X + HY reactions[13] and draws upon the DIM calculations on $F + H_2$ by Tully.[33] Near the interaction region, we see that reaction on the $^2\Sigma_{1/2}$ curve leads from ground state reactants to ground state products with only a small barrier, whereas reaction along the $^2\Pi_{3/2}$ or $^2\Pi_{1/2}$ curve passes through a much larger barrier resulting from an avoided crossing. Near either asymptote, the potential energy curves are similar to the well-studied interaction between a ^1S and a ^2P atom.[36] In this region, where the spin–orbit interaction in the ^2P atom is much larger than the intermolecular potential, it is more appropriate to label the three curves only with Ω, the projection of the total electronic angular momentum on the inter-

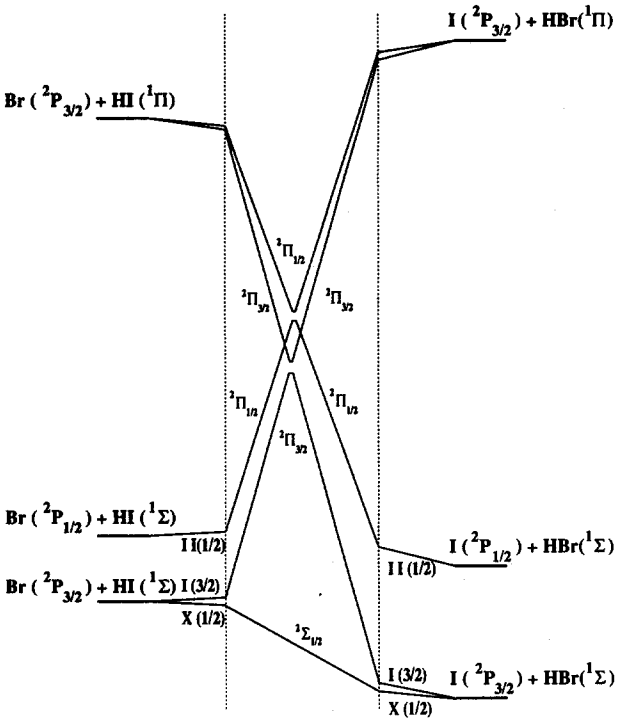

FIG. 10. Correlation diagram for the reaction Br + HI, assuming $C_{\infty v}$ symmetry. The relative spacing of asymptotic levels are approximately to scale. The region between the dotted lines is where Hund's case (a) is appropriate. Adapted from the correlation diagram in Ref. 12.

nuclear axis, since Ω is a good quantum number but Λ (projection of the orbital angular momentum only) is not. Thus, in the asymptotic region, Hund's case (c) applies. The three curves are typically labeled X(1/2), I(3/2), and II(1/2), in order of increasing energy. The two $\Omega = 1/2$ states are linear combinations of $^2\Sigma_{1/2}$ and $^2\Pi_{1/2}$ states, while the $^2\Pi_{3/2}$ state is the only $\Omega = 3/2$ state. The same notation is appropriate for the reactant and product valleys of collinear X + HY reactions. In the HX + Y product valley, the X(1/2) and I(3/2) curves eventually correlate to $Y(^2P_{3/2}) + HX$, whereas the II(1/2) curve correlates to $Y^*(^2P_{1/2}) + HX$. We therefore expect the photoelectron spectrum of XHY^- to show transitions to a maximum of three low-lying electronic potential energy surfaces in the HX + Y product valley.

This is most likely the origin of the three peaks in the FHI^-/FDI^- photoelectron spectra. The correlation diagram in Fig. 10 shows that as HF is brought up to an I atom, the degenerate $^2P_{3/2}$ state is split and the $^2P_{1/2}$ state experiences a repulsive interaction. In our spectra (Figs. 4 and 5), the two peaks X and Y separated by 0.154 eV are assigned transitions to the X(1/2) and I(3/2) states, respectively, which both asymptotically correlate to $I(^2P_{3/2}) + HF$. Peak Z at the lowest electron energy lies 1.05 eV from peak X. This is slightly larger than the I atom spin–orbit splitting and is assigned to a transition to the II(1/2) state which asymptotically correlates to $I^*(^2P_{1/2}) + HF$.

Haberland[37] has shown that of the three potential energy curves resulting from the interaction between a ^1S and an ^2P atom, one curve can be determined if the other two are known provided that the spin–orbit interaction is assumed to be independent of internuclear distance. In the Hund's case (c) limit, one obtains

$$V_{\mathrm{I}}(R) = 2[V_{\mathrm{II}}(R) - \Delta], \tag{3}$$

where Δ is the spin–orbit splitting in the ^2P atom, R is the internuclear distance, and V_{I} and V_{II} are the potential energies of the upper two curves relative to the X(1/2) curve. We can apply this formula to the three peaks in the FHI^- photoelectron spectrum. In this case, $\Delta = 0.943$ eV (the iodine spin–orbit splitting) and the splitting between peaks X and Z is $V_{\mathrm{II}} = 1.045$ eV. Equation (3) yields $V_{\mathrm{I}} = 0.205$ eV, which should be compared to the experimental spacing of 0.154 eV between peaks X and Y. Somewhat better agreement with experiment is obtained using the more accurate equations from which (3) is derived[37] that are appropriate for the intermediate region between the Hund's case (c) and (a) limits. In either case, the reasonable agreement with experiment supports our assignment of the three peaks to three electronic states in the I + HF product valley.

In the $BrHI^-$ and $ClHI^-$ photoelectron spectra, vibrational progressions from only two electronic states are apparent. The interval between the electronic states in the $ClHI^-$ spectrum is equal to the I atom spin–orbit splitting, whereas the interval in the $BrHI^-$ spectrum is slightly less. This suggests that in the region of the product valley probed by our experiment, the interaction between the I and HCl or HBr molecule is not strong enough to produce a resolvable splitting of the degenerate $I(^2P_{3/2})$ state. However, in both spectra, the peaks in the progression from transitions to the lower electronic state are broader than in the excited-state progression. We suggest that the increased width in the former peak results from the splitting of the degenerate $I(^2P_{3/2}) + HX$ state but the splitting is smaller than the widths of the individual transitions. This would mean that the peak observed is an envelope of two broad transitions, whose individual widths are probably comparable to the II(1/2) transition. The ground state peaks in the $ClHI^-$ spectrum are noticeably broader than in the $BrHI^-$ spectrum, indicating either a larger splitting of the I atom electronic degeneracy in the [ClHI] complex or a more repulsive interaction in the I + HCl product valley (see the next section).

In summary, as far as electronic effects are concerned, the interaction between I and HF in the region of the neutral surface probed by photodetachment of FHI^- is stronger than the I + HBr and I + HCl interaction probed in the $BrHI^-$ and $ClHI^-$ spectra. Two effects may contribute to this. The dipole moment of HF is considerably higher than for HBr or HCl (1.82 D vs 0.82 D, 1.08 D).[38] In addition, the bond length in HF is much less than in HBr or HCl (0.917 Å vs 1.414 Å, 1.275 Å).[39] We therefore might expect a shorter interhalogen distance in FHI^- than in $BrHI^-$ or $ClHI^-$. This means that subsequent to photodetachment, the spherical symmetry of the I atom will be most strongly perturbed by the neighboring HX molecule in the case of FHI^-. The larger electronic effects seen in the FHI^- spectrum are reasonable in light of these considerations.

A final point of interest is that the two vibrational progressions in the $BrHI^-$ (and $BrDI^-$) spectrum have similar intensity distributions. The peak spacings in each progression are also similar and are slightly less than the vibrational frequency in isolated HBr (DBr), although this difference is more noticeable in the excited state progression. This indicates that in the geometry probed by our experiment, the distortion of the HBr bond in the [BrHI] complex is approximately independent of the I atom electronic state, and suggests that the ground and excited electronic potential energy surfaces are not very different in the I + HBr product valley. It would clearly be of great interest to probe the excited Br + HI potential energy surfaces in the region of the barrier, as this is where the largest differences among the various surfaces are expected. This possibility is discussed below.

D. Time dependent simulation

The discussion in Sec IV B presents a qualitative explanation for the structured spectrum observed in the $BrHI^-$ photodetachment experiment. The simple one-dimensional calculations provide Franck–Condon stick spectra within a familiar bound–bound eigenstate framework. However, an essential aspect of this experiment is that the neutral [BrHI] complex dissociates rapidly. Our spectra offer a good deal of dynamical information concerning this process, largely through the peak widths. In order to extract this information we must include at least the dissociative degree of freedom in our simulations. As in our analysis of the $BrHBr^-$ and IHI^- spectra, we assume that no bending excitation in the neutral complex results from photodetachment and we confine ourselves to a two-dimensional treatment in which only the ν_1 and ν_3 stretching motions are considered.

In our treatment of $BrHBr^-$ and IHI^- photoelectron spectra, we used an adiabatic approximation to separate the bound (ν_3) and dissociative (ν_1) degrees of freedom, justified because of the different time scales for the two motions in a heavy–light–heavy system.[2,3] While the $BrHI^-$ and $BrDI^-$ spectra could be simulated in the same way, this approximation is not so straightforward for asymmetric systems.[40] Alternatively one can exactly solve the two-dimensional problem with a coupled channel collinear scattering calculation.[11(b),41] However, we choose to use the time-dependent wave packet propagation method which also yields an exact solution. The time-dependent picture reveals the relationship between our experimental spectrum and the short time dynamics of the half reaction initiated on the neutral reaction surface in a more intuitive manner than the time-independent analyses.

The practical difference between the two approaches is this. In time-independent treatments, each of the many scattering states over a range of energies are solved for, and the simulated spectrum is described by the square of the overlap of the anion wave function with each of these neutral eigenfunctions. The time-dependent perspective is based on the fact that the photoelectron spectrum is equivalently expressed as the Fourier transform of a time autocorrelation function $C(t)$:

$$\sigma(E) \propto \int_{-\infty}^{\infty} \exp(iEt/\hbar) C(t) dt. \tag{4}$$

This complex function $C(t)$ monitors the overlap of a moving wave packet with the initial wave packet as a function of time

$$C(t) = \langle \phi(0) | \phi(t) \rangle. \tag{5}$$

The initial wave packet, $\phi(0)$, in this case is defined as the ground state vibrational wave function of the anion, assuming the electronic dipole moment operator is a constant over the range of this wave function. The motion of the wave packet subsequently on the neutral surface is described by

$$|\phi(t)\rangle = e^{-i\hat{H}t/\hbar} |\phi(0)\rangle, \tag{6}$$

where $e^{-i\hat{H}t/\hbar}$ is the time propagation operator and $\hat{H}$ is the Hamiltonian for the upper (neutral) surface. In this way the spectrum is simulated by simply performing the wave packet propagation and transforming the resultant autocorrelation function. This dynamical approach to molecular spectroscopy has been applied by other workers to the analysis of absorption and emission,[42,43] fluorescence,[44] photoelectron[45,46] and Raman[47] experimental spectra.

The propagation scheme implemented here is due to Kosloff and Kosloff;[48] we use the Fourier method for evaluation of the Hamiltonian and second order differencing to approximate the propagator. An advantage of the Fourier representation of the kinetic energy is that a relatively sparse spatial grid can be used. Convergence has been tested in each case by doubling the density of grid points along each dimension and halving the propagation time step. The parameters used for each calculation are shown in respective captions.

The concepts involved in spectral analysis based on the autocorrelation function have been described admirably elsewhere.[14,43] The application of these concepts to our results will be undertaken in two steps. We first discuss the features that appear in the autocorrelation function when considering the bound ν_3 degree of freedom alone. We then consider the extra features that result from a two-dimensional analysis which includes the second (ν_1), dissociative degree of freedom.

1. One-dimensional time-dependent treatment of the $BrHI^-$ spectrum

The features of the ground state progression in the $BrHI^-$ photoelectron spectrum have been explained in terms of eigenvalues of a one dimensional double well potential in Sec. IV B. In a time dependent picture the key to understanding this structure lies in the autocorrelation function, $\langle \phi(0) | \phi(t) \rangle$, and its relationship to the motion of the wave packet. Figure 11 shows the modulus of the autocorrelation function calculated for the BrHI system, using the same anion ground state wave function and the same one dimensional cut of the neutral Br + HI LEPS surface as was used in the time independent treatment. Figure 11 also shows the resulting photoelectron spectrum obtained by the Fourier transform of the complex $C(t)$ function. A comparison of this simulation and the time independent one in Figure 9 shows that they are identical, as we should expect be-

cause the two one-dimensional treatments are exact and equivalent.

Figure 11 (top) shows that the correlation between the initial wave packet, $\phi(0)$ and the wave packet at time t, $\phi(t)$, falls off rapidly in the first 10 fs after $t = 0$. This indicates that the packet moves quickly away from the Franck–Condon region, which in turn indicates that there is considerable excitation in this ν_3 mode. In fact, the faster the fall of $|C(t)|$ from unity at $t = 0$, the longer the vibrational progression, or the larger the bandwidth in the photoelectron spectrum. The most noticeable feature of $|C(t)|$ at longer times is the oscillatory, or recurrence, structure. A recurrence occurs when the wave packet $\phi(t)$ returns to the Franck–Condon region. The recurrence structure in $|C(t)|$ corresponds to the observation of discrete structure, rather than a featureless continuum, in the photoelectron spectrum. The $|C(t)|$ in Fig. 11 has periodic structure out to infinite time; this serves only to make the peaks in the photoelectron spectrum infinitely narrow, which is to be expected for a treatment that includes only a single bound degree of freedom. As pointed out earlier, the peaks in the $BrHI^-$ photoelectron spectrum are not equally spaced because the reaction potential surface cut does not have a single minimum. The motion of the wave packet in this potential cannot then be described as a coherent single frequency oscillation. The complex structure shown in Fig. 11 and the fact that the height of the first recurrence is not unity are due to this effect which is comparable to dephasing of a wave packet moving in an anharmonic potential well. It is important to emphasize again that this peculiar double oscillatory feature is a result of the shape of the potential along the bound ν_3 coordinate, and is not related to the dissociative degree of freedom.

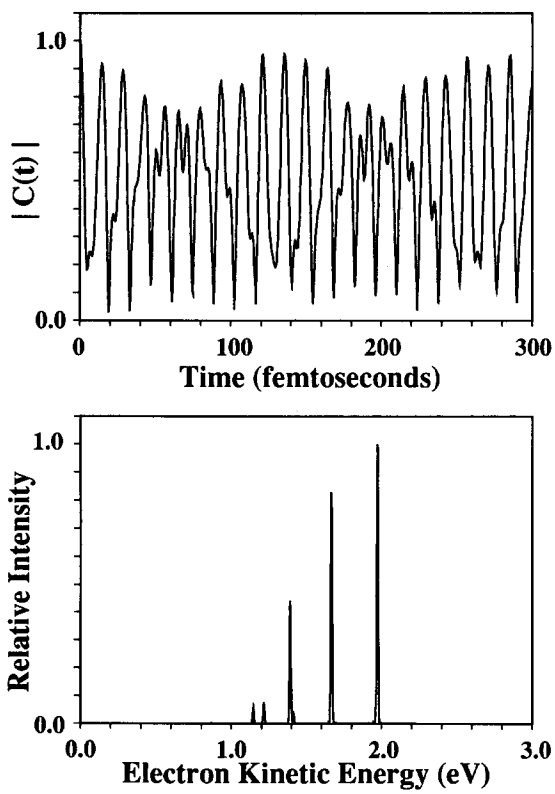

FIG. 11. Absolute value of autocorrelation function, from one-dimensional propagation, for $BrHI^-$ (top) and the simulated photoelectron spectrum which results from the Fourier transform of this autocorrelation function (bottom). Propagation carried out for 16384 time steps, with $\Delta t = 1.0$ a.u., and a 64 point spatial grid along y ($= R_{H\text{-}Br}$) between 0.79 and 3.4 Å.

The finite propagation of the wave packet in time, up until $t = t_{max}$, leads to a finite resolution of the simulated photoelectron spectrum. In principle this is given, in atomic units, by $\Delta E = \pi/t_{max}$.[49] However, in practice, if the autocorrelation has not fallen to zero by t_{max} then its Fourier transform will show artificial high frequency oscillations; this problem is rectified by convolution with a window function.[50] The choice of a Gaussian window function is equivalent to convoluting the stick spectrum in energy with a Gaussian energy resolution function. This operation has been performed to the one dimensional autocorrelation Fig. 11 (top) to yield the simulated spectrum (bottom) so that the sticks have FWHM of 10 meV.

2. Two-dimensional analysis of the $BrHI^-$ and $BrDI^-$ photoelectron spectra

(*a*) *Method.* The extension to higher dimensions of the time dependent approach is conceptually simple. The propagator now allows for motion of the initial wave packet along two dimensions, namely the two stretching coordinates of the linear triatomic. The autocorrelation is calculated in the same manner and the transformation to a photoelectron spectrum simulation is identical to that described above. The two dimensional treatment allows us to assign physical meaning to the peak widths. In the following calculations we aim to simulate the full ground X(1/2) state progression for the photoelectron spectra of $BrHI^-$ and $BrDI^-$, using the published potential energy surface. At present we neglect the effects of the nearby I(3/2) surface, discussed in Sec. IV C, on the X(1/2) progression in the photoelectron spectra. We shall discuss the agreement with the experimental spectra and comment on the interpretation of the peak widths.

The propagation is performed on the *effective collinear* reaction surface derived from the BP LEPS surface. To extract the effective collinear surface from the supplied LEPS function of all three internal coordinates, the bending angle is considered fixed at 180°, and the zero point energy due to bending motion is included at every grid point.[3] The zero point bend energy is calculated in an harmonic approximation. This approach is in the spirit of the reduced dimensionality model of Bowman.[51] It is justified as long as little or no bending excitation is expected in the photoelectron spectrum. This is a reasonable assumption so long as the ion is linear and the minimum energy path on the neutral surface is collinear. The Broida and Persky LEPS parameters are not at any time adjusted to fit the experimental spectrum.

The spatial grid used in the calculation is set up on the mass scaled coordinates, x and y defined in the caption of Fig. 6, so that the kinetic energy operator is diagonalized. μ_{HBr} is the appropriate reduced mass for describing motion on this surface. The anion potential surface is then the sum of the Morse potential (1) along y and a harmonic oscillator

with frequency ν_1 along x. The equilibrium point of the anion potential is fixed at the best fit values found from the one dimensional analysis, namely $y_e = 1.55$ Å and $x_e = 27.1$ Å. The initial wave packet is set equal to the ground state eigenfunction of this anion potential. Unfortunately there is no matrix isolation or calculated value for the ν_1 fundamental; this frequency would indicate the extent of the initial wave packet along the dissociation coordinate x. However combination bands have been seen in the matrix isolation spectra of $BrHBr^-$ and IHI^- yielding ν_1 values for these ions of 164 and 121 cm^-, respectively.[52] The calculated ν_1 frequency for $FHCl^-$ is lower than the observed ν_1 of both FHF^- and $ClHCl^-$.[16,26] Furthermore, the ν_1 frequency should be approximately unchanged upon isotopic substitution of the hydrogen. We therefore set ν_1 for $BrHI^-/BrDI^-$ at 100 cm^{-1}; only minor changes in the resulting simulation occur if we double this frequency.

This initial wave packet is propagated on the upper surface for 320 femtoseconds. The calculation is checked for convergence with respect to grid size and time step. The potential function has been shelved at extremely high values (5 eV above the I + HBr energy zero), otherwise a prohibitively small time step is required for a stable propagation.[53] For the two-dimensional simulation shown here utilizing a 128×64 grid, the entire calculation took 7 CPU h on a VAX 8650. As observed by Kosloff,[15] the numerical method is particularly suitable for vectorization on a supercomputer; the same calculation required only 3.3 CPU min on a Cray X/MP 14. Considerable reduction in run time can be achieved by employing absorbing grid boundaries which immediately allows use of a less extensive grid.[53] By this device it was possible to perform propagations to a picosecond on a 64×32 grid and examine resonances to higher energy resolution; these computations required 2.5 CPU min total on the Cray.

(*b*) *Results and Discussion.* The calculated autocorrelation functions for BrHI and BrDI wave packet dynamics are shown in Fig. 12. The oscillatory structure out to 60 fs is strongly reminiscent of the autocorrelation function calculated in one dimension (see Fig. 11). However it is quite clear that the inclusion of motion along the dissociation coordinate leads to damping of the oscillations in the autocorrelation function over this time range. Each succeeding time that the wave packet bounces back along the HBr coordinate to the Franck–Condon region, it has progressed further along the x coordinate and as such has diminishing overlap with $\phi(0)$. A single recurrence in the autocorrelation is necessary, but sufficient, to yield oscillatory structure in the energy spectrum, as shown by Imre for the photodissociation of H_2O.[43] If all ν_3 states supported by the one dimensional cut dissociated by the same direct mechanism one would expect essentially the one dimensional result convoluted with a single Gaussian envelope damping function to give the two dimensional autocorrelation function. The calculated function shown in Fig. 12(a) clearly has a more complicated form; there is long time structure which has a qualitatively different form from the shorter time structure. Analysis of the wave packet dynamics and the Fourier transform of the time autocorrelation function show that the ν_3

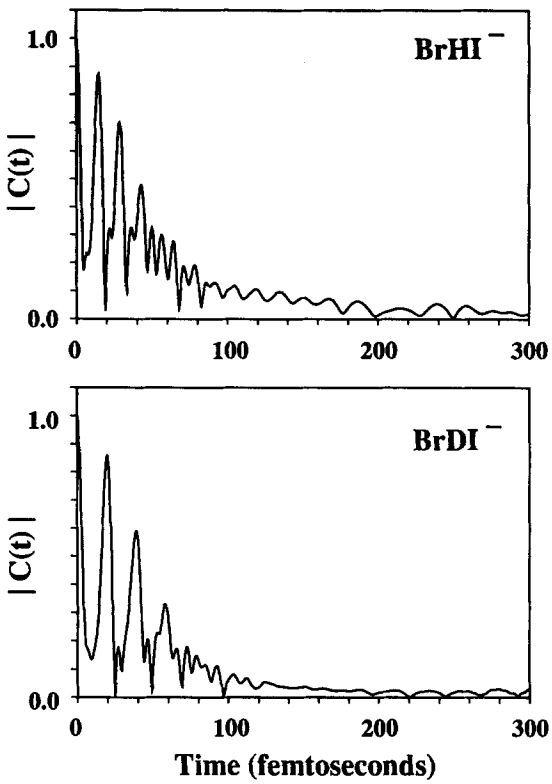

FIG. 12. Absolute value of autocorrelation function, from two-dimensional propagation, for (a) $BrHI^-$ and (b) $BrDI^-$. Calculation parameters given with Fig. 13.

states have widely differing lifetimes.

Figure 13 explicitly shows how the initial wave packet $\phi(0)$ evolves as a function of time on the Br + HI surface. The modulus of $\phi(t)$ is plotted at several times ranging from $t = 0$ to $t = 966.4$ fs. The plots show the regions of the potential sampled by the wave packet, the mode or mechanism of dissociation, and the branching ratio between the arrangement and vibrational channels. The time-dependent function $\phi(t)$ represents the evolution of a coherent superposition of scattering eigenfunctions Ψ_E weighted by $\langle \phi(0) | \Psi_E \rangle$. Although $\phi(t)$ and the photoelectron spectrum are uniquely related through Eq. (4), we point out that, in contrast to a short-pulse laser absorption experiment, such a superposition is *not* created in our photoelectron spectroscopy experiment. Instead, each photodetachment event results in a well-defined neutral scattering state Ψ_E with probability $|\langle \phi(0) | \Psi_E \rangle|^2$. However, the plots of $\phi(t)$ show what would occur if the initial wave packet $\phi(0)$ were created on the neutral potential energy surface and therefore provide considerable insight into the dissociation dynamics of the [BrHI] complex.

The first picture ($t = 0$ fs) shows that the bulk of the initial wave packet's amplitude is in the I + HBr exit valley, although $\phi(0)$ does have some amplitude at the saddle point region of the potential surface and therefore will have finite overlap with states localized in the HI valley. In the first few femtoseconds a small fraction of the wave packet breaks

away upwards into the saddle point region while the rest moves downwards. The period of oscillation of this major component of the packet along the y coordinate is essentially that of diatomic HBr ($\tau_{HBr} = 12.6$ fs). This is the dominant periodicity shown in the autocorrelation. The second frame shows the packet after $\sim 1.5\,\tau_{HBr}$ where $|C(t)|$ goes through a minimum. As noted for the one dimensional autocorrelation, the anharmonicity of the potential governing this fast oscillation along the y coordinate leads to a more complicated periodic structure. On each of the first few occasions that the major component of the packet returns to the soft wall, a fraction crosses the ridge between product and reactant valleys (seen in the pictures at $t = 20.1$ and 40.3 fs).

Over the first 60 fs the major part of the wave packet moves barely perceptibly along the dissociation coordinate. However at later times we see this motion becomes more dominant; the overlap of this component of $\phi(t)$ with $\phi(0)$ becomes much smaller, and thus its contribution to the shape of the autocorrelation is diminished. Therefore the autocorrelation at times later than 60 fs slowly loses resemblance to the earlier pattern and that seen in the one dimensional simulation. The pictures at longer times (e.g., at $t = 201.3$ and 261.7 fs) show that the component of the wave packet which exits through the product valley spreads along x. From the leading edge (at higher x) to the tail there is an increasing number of nodes along the y direction. This suggests that states with higher ν_3 excitation proceed more slowly along the dissociation coordinate. This is in accord with our simulations on $BrHBr^-$,[3] and is manifested in the narrower linewidths of the [BrHI] $v_3 = 3$ and $v_3 = 5$ peaks

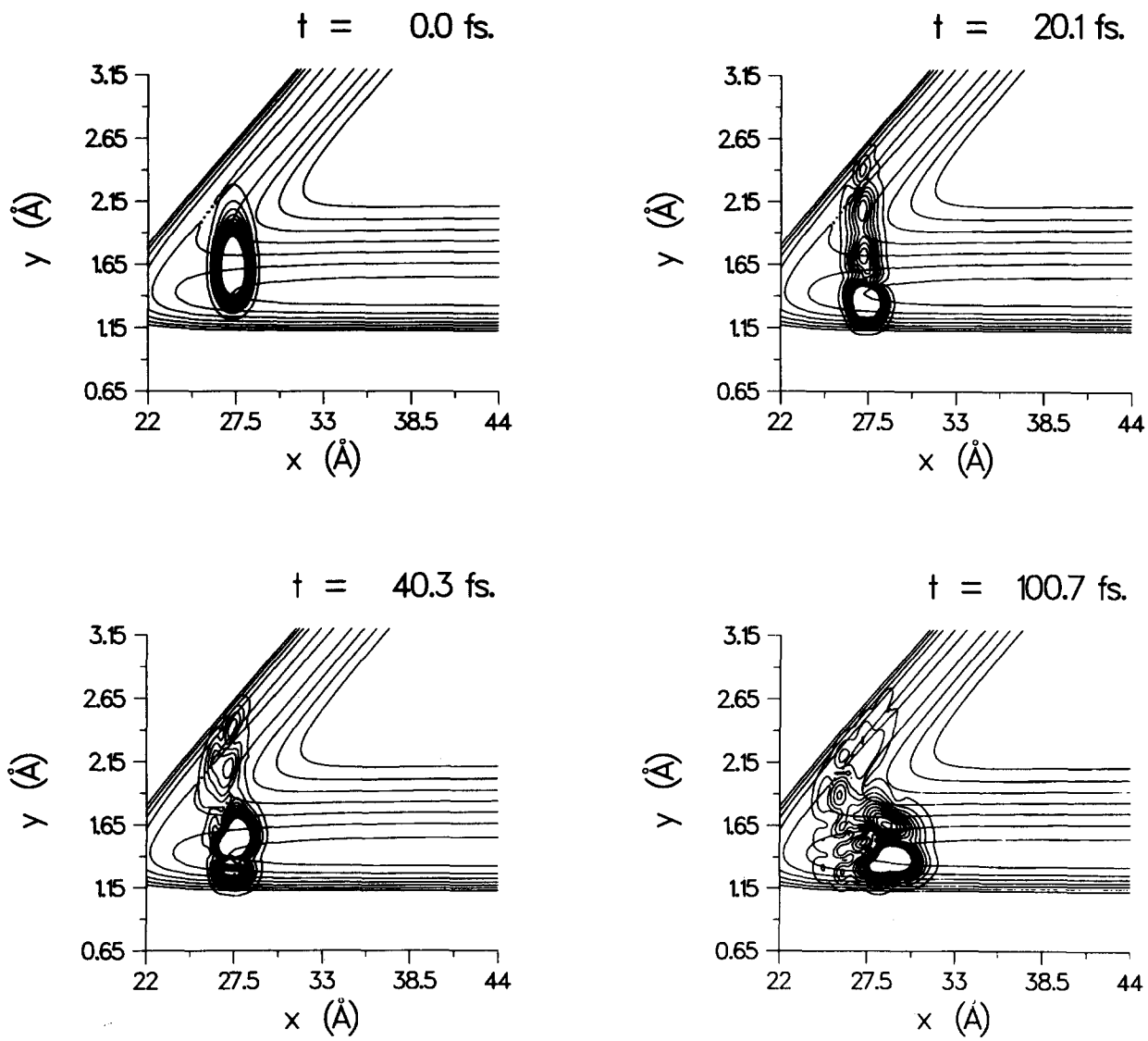

FIG. 13. Wave packet dynamics for the [BrHI] system. Equally spaced contours of $|\phi(t)|$ are shown at times indicated on each frame; the highest value contours are omitted for clarity. Also shown are contours of the *effective collinear* potential energy surface, shown in Fig. 6. Figure plotted in mass scaled coordinates (see the text and Fig. 6); the y axis has been expanded here. Propagation performed over 10240 time steps, with $\Delta t = 1.3$ a.u., and a spatial grid with 128×64 points along x and y, respectively. The final wave packet shown (966.4 fs) was calculated in a separate propagation, using same grid and Δt, but with an absorbing function applied at grid boundaries (see the text and Ref. 53). In this last plot the contouring resolution has been increased.

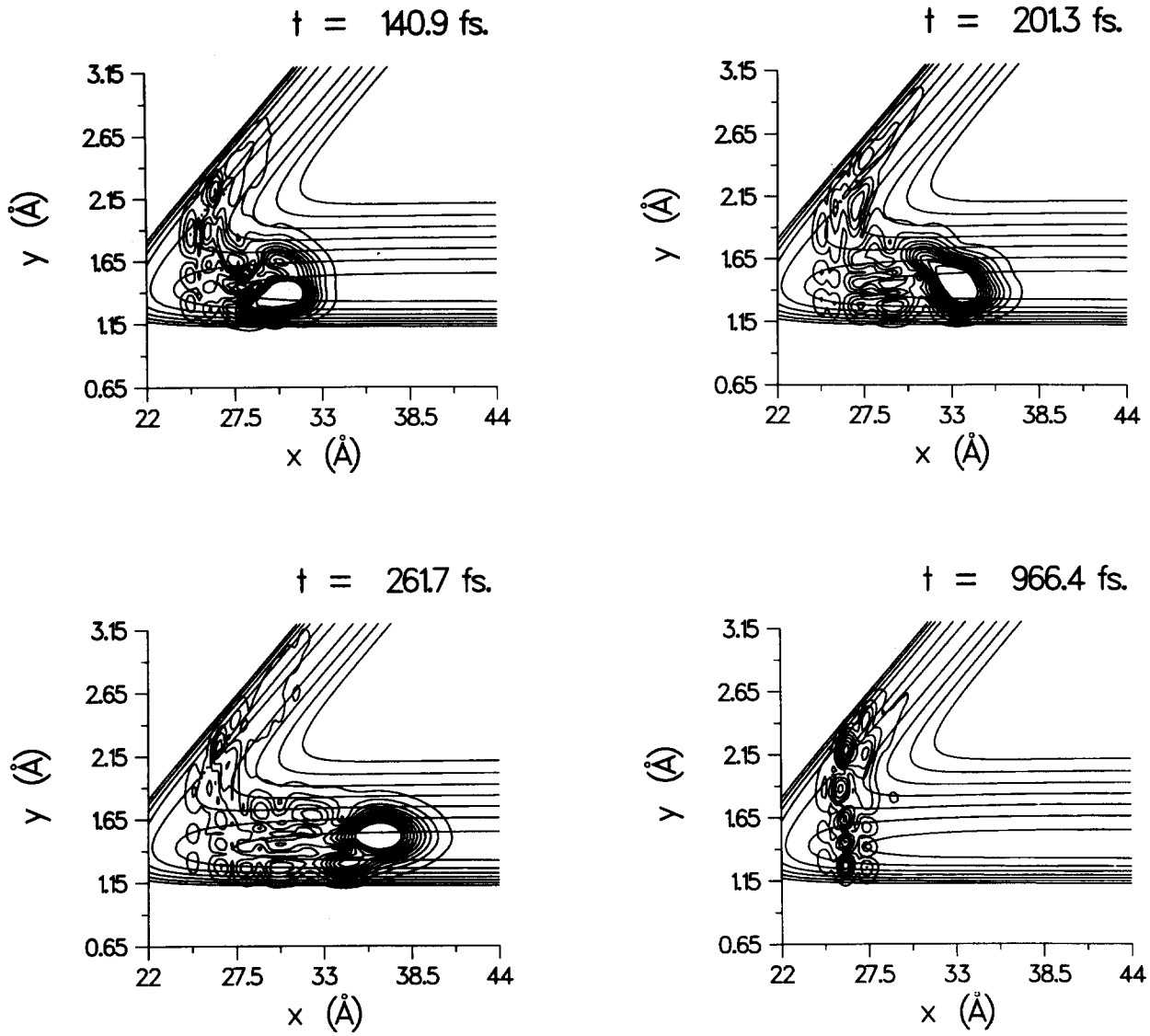

Fig. 13 (*continued*).

in the simulated photoelectron spectrum [Fig. 14(a), Table III]. Moreover, notice the series of later time pictures show some components of the wave packet that remain localized in coordinate space for extended periods of time (e.g., at $t = 201.3$, 261.7, and 966.4 fs). These correspond to a weighted superposition of quasistationary states or resonance states; the dominant resonance states seen have $v_3 = 4$. These are manifested in the autocorrelation at long time as oscillations modulated by a second frequency. In the simulated photoelectron spectrum the resonances appear as a series of closely spaced (~ 18 meV or $\sim 150\ \text{cm}^{-1}$) peaks at 1.21 eV electron energy. However they are not resolved individually when the simulation is convoluted with the experimental resolution function [Fig. 14(a)]. The positions of these resonances, which have not decayed by the end of a picosecond in this two dimensional simulation, are listed in Table III. These states can be projected out and their individual mode of decay can be studied by time-dependent propagation as shown by Bisseling *et. al.*[53]

The differing lifetimes of each vibrational state, and the resonance phenomenon supported by the potential energy surface used in this simulation, explain the complex decay of the autocorrelation function. The simulated photoelectron spectra for $BrHI^-$ and $BrDI^-$ have been convoluted with the true instrument resolution function (given in Ref. 3) and are shown in Fig. 14 where they are superimposed on the experimental spectra. It is quite clear that the *experimental* spectra do not show many of the features discussed above, and the autocorrelation functions leading to these spectra should be much simpler than that shown in Fig. 12. The spacing of the peaks and the qualitative trends in peak width, namely decreasing width with greater vibrational excitation, are in good agreement with the experimental spectra. However the discrepancy in the magnitudes of the widths is striking, and the variation of width is much less noticeable in the experimental spectrum as opposed to the halving of linewidth seen between the simulated $v_3 = 0$ and $v_3 = 3$ peaks. Moreover, we have shown that in a two dimensional

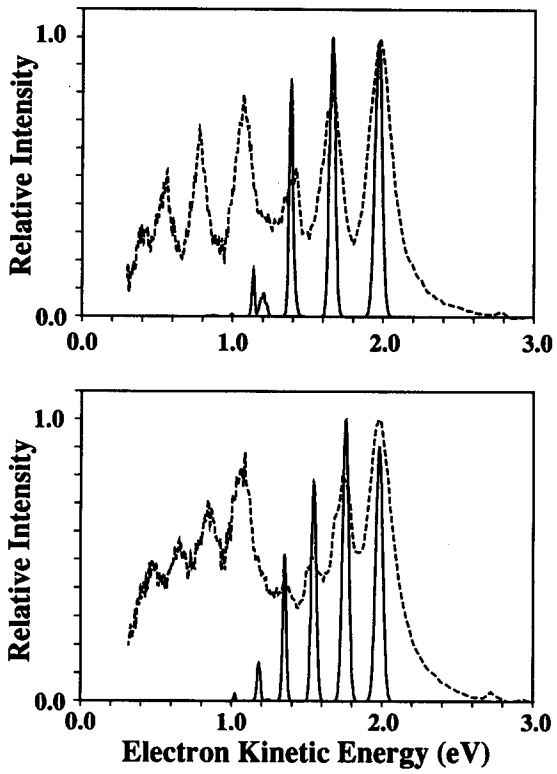

FIG. 14. Simulated photoelectron spectrum (solid) for (a) $BrHI^-$ and (b) $BrDI^-$ resulting from two-dimensional calculation. The simulations have been shifted so 0–0 bands line up (see the text) and convoluted with the experimental resolution function. The experimental spectra are also shown (dashed).

TABLE III. Results of exact quantum collinear simulation of photoelectron spectra of $BrHI^-$ and $BrDI^-$ using BP LEPS surface with zero point bend included.

	Electron kinetic energy (eV)[a]	ν_3 assignment	Width (meV)
$BrHI^-$	1.970	0	43
	1.662	1	36
	1.447	2	<4
	1.429	2	<4
	1.416	2	<4
	1.408	2	<4
	1.388	3	15
	1.230	4	<4
	1.211	4	<4
	1.192	4	<4
	1.176	4	<4
	1.143	5	8
	0.998	6	<4
$BrDI^-$	1.975	0	41
	1.751	1	38
	1.539	2	30
	1.346	4	10
	1.262	5	<4
	1.242	5	<4
	1.227	5	<4
	1.184	6	<4
	1.171	6	<4
	1.017	8	<4

[a] Entire simulation shifted to higher electron energy by 0.062 (0.058) eV for $BrHI^-$ ($BrDI^-$) to line up with experimental bands.

simulation, the BP LEPS surface supports resonance states which should give rise to sharp peaks in the spectrum, although the intensity of these peaks is expected to be small. These are not evident in the experimental profiles. Thus, in time-independent language, the experimental peaks all appear to be from direct scattering states on the Br + HI surface. Lastly, the origins of the simulated photoelectron bands must be shifted to higher electron kinetic energy by approximately 60 meV to match with the experimental ones. This shift is just larger than the cumulative error in the reported thermochemical and spectroscopic data used to link the energy zeros of ion and neutral.

We would like to be able to use the discrepancies between the simulated and experimental spectra, in particular the differences in the peak widths, to learn about the Br + HI potential energy surface. One might argue that the broad experimental peaks result from the multiple electronic states of the neutral complex accessible via photodetachment. In Sec. IV C, we have argued that each peak in the progression at higher electron kinetic energy could be split due to an electronic interaction between the dipole of the HBr and the open shell iodine atom. In the [FHI] system where the electronic interaction is largest and the components are resolved, some differences in peak width are seen for the three states [see Table I(c)]. In the case of [BrHI] less of a difference is expected in the peak shape and width among the three states. It is probable that the splitting is in fact a fairly small part of the width, the major part of which is intrinsic to the transition to a dissociative state.

A similar discrepancy between the simulated and experimental peak widths was also seen in our analysis of the $BrHBr^-$ photoelectron spectrum when we assumed a LEPS potential energy surface for the Br + HBr reaction.[3] We therefore developed a more flexible functional form for an effective collinear Br + HBr surface which allowed the construction of a surface with a steeper minimum energy path in the Franck–Condon region. Simulations on this surface did reproduce the broad peak widths observed in the $BrHBr^-$ spectrum. A similar modification may be required for the BP Br + HI surface; i.e., the surface may not be steep enough in the I + HBr exit valley. Another possibility is that the minimum energy path on the correct Br + HI surface is not collinear, in which case the effective collinear approach is not appropriate and full three-dimensional simulations are required to accurately simulate the photoelectron spectrum. In any case, while it is somewhat risky to draw conclusions on the possible defects of a reactive potential energy surface based on an effective collinear analysis, this type of analysis provides an important first step in relating the features of the $BrHI^-$ photoelectron spectrum to the Br + HI potential energy surface.

Two variations on this experiment should provide considerably more information on the Br + HI reaction. $BrHI^-$ in its ground vibrational state has good Franck–Condon overlap with the I + HBr product valley. This is certainly an important region of the potential energy surface as it plays a major role in determining how the energy released in the reaction is partitioned among product degrees of freedom. However, we would also like to probe the reac-

tant side of the potential energy surface, particularly the barrier. In Fig. 8, note that the neutral levels with $v_3 > 4$ span both valleys of the potential energy surface. While transitions to these levels from the $v_3 = 0$ level of $BrHI^-$ are very weak, transitions originating from the $v_3 = 1$ level of the ion are considerably stronger. A simulated photoelectron spectrum assuming $BrHI^-$ with $v_3 = 1$ is shown at the top of Fig. 15. The appearance of this spectrum is quite different from the simulation in Fig. 14 and shows intense peaks due to transitions to these higher neutral ν_3 levels. Hence, vibrational excitation of the ion provides an elegant means of probing the reactant side of the Br + HI surface. In general, vibrational excitation of various modes of the ion is akin to varying the distribution of reactant energy in a state-to-state scattering experiment.

The simulated spectrum at the top of Fig. 15 is convoluted with the experimental resolution of our photoelectron spectrometer. The spectrum at the bottom of Fig. 15 assumes a constant experimental resolution of 4 meV (35 cm^{-1}) and shows correspondingly more structure. For example, the $v_3 = 4$ peak splits into four closely spaced peaks which are actually resonance states quasi-bound along the ν_1 coordinate. The appearance of these was discussed in the time dependent section above. Thus, a spectrometer with somewhat higher resolution has the capability to reveal considerably more detail concerning the Br + HI potential energy surface. We currently have such an instrument:[54] a threshold photodetachment spectrometer with a resolution of 3 cm^{-1}. Recent results on IHI^- have already shown vibrational features of the [IHI] complex that were obscured at lower resolution.[55,56] Studies of asymmetric systems with this instrument will be undertaken in the near future.

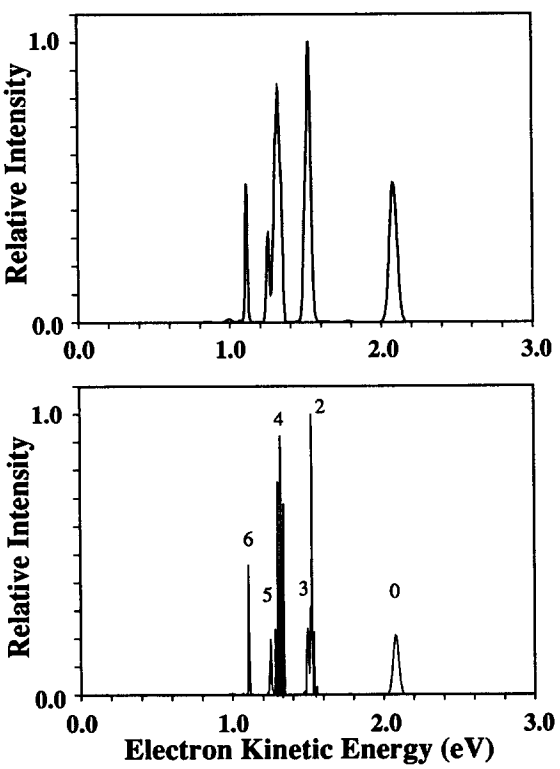

FIG. 15. Simulated photoelectron spectrum for $BrHI^-$ prepared in the (0, 0, 1) state. Simulation has been convoluted with (top) our spectrometer's experimental resolution function and (bottom) with a constant energy resolution of 4.3 meV. Bands are labeled by their effective v_3 quantum numbers. Numerical parameters for the simulation are $\Delta t = 1.3$ a.u., $t_{max} = 960$ fs, spatial grid 64×32 points over range $x = 22$–35 Å and $y = 0.95$–3.1 Å.

V. SUMMARY

Photoelectron spectra for the asymmetric bihalide anions XHI^- and XDI^- (X = Br, Cl, F) have been obtained in order to learn about the transition state region on the neutral X + HI potential energy surfaces. In the case of $BrHI^-$ and $ClHI^-$, the spectra show resolved vibrational progressions assigned to the ν_3 hydrogen stretching mode of the neutral [XHI] complex. In all the spectra, transitions are observed not only to the ground state reactive potential energy surface, but also to electronically excited surfaces which correlated asymptotically to $HX + I(^2P_{3/2}, ^2P_{1/2})$. The $BrHI^-$ and $BrDI^-$ spectra are analyzed in detail using an approximate geometry for the ion and a model potential energy surface for the Br + HI reaction. A one-dimensional analysis is used both to simulate the peak positions and intensities of the $BrHI^-$ and $BrDI^-$ spectra and to understand the appearance of the other XHI^- spectra. We have also performed a two-dimensional quantum collinear simulation of the spectra of $BrHI^-$ and $BrDI^-$ via the wave packet propagation technique. The results of this time dependent simulation provide further insight into the origin of the structure seen in our spectra. The simulated peaks are narrower then the experimental peaks; this is discussed in terms of properties of the model Br + HI surface and approximations in the analysis.

ACKNOWLEDGMENTS

We would like to acknowledge Dr. Soo-Y. Lee for helping us start the time dependent simulation of the $BrHI^-$ spectrum by providing us with routines for the Kosloff algorithm in one dimension. We also thank Professor M. Shapiro for useful discussions and Professor P. Botschwina for communicating his results on $FHCl^-$ prior to publication. Support from the Air Force Office of Scientific Research under Contract No. AFOSR-87-0341 is gratefully acknowledged. D. M. N. thanks the Research Corporation and the Donors of the Petroleum Research Fund, administered by the American Chemical Society, for support.

[1] R. B. Metz, T. Kitsopoulos, A. Weaver, and D. M. Neumark, J. Chem. Phys. **88**, 1463 (1988).
[2] A. Weaver, R. B. Metz, S. E. Bradforth, and D. M. Neumark, J. Phys. Chem. **92**, 5558 (1988).
[3] R. B. Metz, A. Weaver, S. E. Bradforth, T. N. Kitsopoulos, and D. M. Neumark, J. Phys. Chem. **94**, 1377 (1990).
[4] G. C. Schatz, J. Chem. Phys. **90**, 3582 (1989); G. C. Schatz, *ibid.* **90**, 4847 (1989).
[5] J. M. Bowman and B. Gazdy, J. Phys. Chem. **93**, 5129 (1989).
[6] B. Gazdy and J. M. Bowman, J. Chem. Phys. **91**, 4615 (1989).
[7] S. E. Bradforth, A. Weaver, R. B. Metz, and D. M. Neumark, *Advances in Laser Science-IV Proceedings of the 1988 International Laser Science Con-*

ference, (American Institute of Physics, New York, 1989), p. 657.
[8] N. Jonathon, C. M. Melliar-Smith, S. Okuda, D. H. Slater, and D. Timlin, Mol. Phys. **22**, 561 (1971); D. H. Maylotte, J. C. Polanyi, and K. B. Woodall, J. Chem. Phys. **57**, 1547 (1972); J. R. Grover, C. R. Iden, and H. V. Lilenfeld, *ibid.* **64**, 4657 (1976); C-C. Mei and C. B. Moore, *ibid.* **70**, 1759 (1979); K. Tamagake, D. W. Setser, and J. P. Sung, *ibid.* **73**, 2203 (1980); D. A. Dolson and S. R. Leone, *ibid.* **77**, 4009 (1982).
[9] C. A. Parr, J. C. Polanyi, and W. H. Wong, J. Chem. Phys. **58**, 5 (1973); D. J. Douglas, J. C. Polanyi, and J. J. Sloan, Chem. Phys. **13**, 15 (1976); I. W. M. Smith, Chem. Phys. **20**, 437 (1977); J. C. Brown, H. E. Bass, and D. L. Thompson, J. Phys. Chem. **81**, 479 (1977); P. Beadle, M. R. Dunn, N. B. H. Jonathon, J. P. Liddy, and J. C. Naylor, J. Chem. Soc. Faraday Trans. 2 **74**, 2170 (1978).
[10] M. Broida and A. Persky, Chem. Phys. **133**, 405 (1989).
[11] M. Baer, J. Chem. Phys. **62**, 305 (1975); J. A. Kaye and A. Kupperman, Chem. Phys. Lett. **92**, 574 (1982); P. L. Gertitschke, J. Manz, J. Römelt, and H. H. R. Schor, J. Chem. Phys. **83**, 208 (1985); J. Manz and H. H. R. Schor, Chem. Phys. Lett. **107**, 549 (1984).
[12] K. Bergmann, S. R. Leone, and C. B. Moore, J. Chem. Phys. **63**, 4161 (1975).
[13] J. W. Hepburn, K. Liu, R. G. Macdonald, F. J. Northrup, and J. C. Polanyi, J. Chem. Phys. **75**, 3353 (1981).
[14] E. J. Heller, J. Chem. Phys. **68**, 3891 (1978); Acc. Chem. Res. **14**, 368 (1981).
[15] R. Kosloff, J. Phys. Chem. **92**, 2087 (1988).
[16] K. Kawaguchi and E. Hirota, J. Chem. Phys. **87**, 6838 (1987); K. Kawaguchi, *ibid.* **88**, 4186 (1988).
[17] P. Botschwina, P. Sebald, and R. Durmeister, J. Chem. Phys. **88**, 5246 (1988); A. B. Sannigrahi and S. D. Peyerimhoff, J. Mol. Struct. Theochem. **165**, 55 (1988); S. Ikuta, T. Saitoh, and O. Nomura, Inorg. Chem. (submitted).
[18] C. R. Moylan, J. D. Dodd, C. Han, and J. I. Brauman, J. Chem. Phys. **86**, 5350 (1987).
[19] L. A. Posey, M. J. DeLuca, and M. A. Johnson, Chem. Phys. Lett. **131**, 170 (1986).
[20] M. L. Alexander, N. E. Levinger, M. A. Johnson, D. Ray, and W. C. Lineberger, J. Chem. Phys. **88**, 6200 (1988).
[21] W. C. Wiley and I. H. McLaren, Rev. Sci. Instrum. **26**, 1150 (1955).
[22] G. Caldwell and P. Kebarle, Can. J. Chem. **63**, 1399 (1985).
[23] H. Hotop and W. C. Lineberger, J. Phys. Chem. Ref. Data. **14**, 731 (1985).
[24] J. W. Larson and T. B. McMahon, Inorg. Chem. **23**, 2029 (1984).
[25] A. B. Sannigrahi and S. D. Peyerimhoff, Chem. Phys. Lett. **112**, 267 (1984).
[26] P. Sebald and P. Botschwina (to be published).
[27] J. E. Bartmess and R. T. McIver, in *Gas Phase Ion Chemistry*, edited by M. T. Bowers (Academic, New York, 1979).
[28] In fact the *effective collinear* surface, which has the zero point energy due to the doubly degenerate bend added at every point (described in Sec. IV D), is shown in Fig. 6. The correction is small but the barrier on this effective surface is 0.84 kcal/mol.
[29] C. M. Ellison and B. S. Ault, J. Phys. Chem. **83**, 832 (1979).
[30] B. S. Ault, J. Phys. Chem. **83**, 837 (1979).
[31] P. L. Houston, Chem. Phys. Lett. **47**, 137 (1977).
[32] J. J. Duggan and R. Grice, J. Chem. Soc. Faraday Trans. 2 **80**, 739 (1983).
[33] J. C. Tully, J. Chem. Phys. **60**, 3042 (1974).
[34] G. C. Pimentel, J. Chem. Phys. **19**, 446 (1951).
[35] Figure adapted for collinear reaction from that appearing in Ref. 12.
[36] See, for example, C. H. Becker, P. Casavecchia, Y. T. Lee, R. E. Olson, and W. A. Lester Jr., J. Chem. Phys. **70**, 5477 (1979), and references therein.
[37] H. Haberland, Z. Phys. A **307**, 35 (1982).
[38] R. D. Nelson, D. R. Lide, and A. A. Maryott, in *CRC Handbook of Chemistry and Physics*, 69th ed., edited by Weast (CRC, Cleveland, 1988), p. E-58.
[39] K. P. Huber and G. Herzberg, *Molecular Spectra and Molecular Structure IV. Constants of Diatomic Molecules* (Van Nostrand, New York, 1979).
[40] J. Römelt, Chem. Phys. **79**, 197 (1983).
[41] D. K. Bondi, J. N. L. Connor, J. Manz, and J. Römelt, Mol. Phys. **50**, 467 (1983).
[42] S. O. Williams and D. G. Imre, J. Phys. Chem. **92**, 3374 (1988).
[43] N. E. Henriksen, J. Zhang, and D. G. Imre, J. Chem. Phys. **89**, 5607 (1988); J. Zhang and D. G. Imre, *ibid.* **90**, 1666 (1989).
[44] D. G. Imre, J. L. Kinsey, R. W. Field, and D. H. Katayama, J. Phys. Chem. **86**, 2564 (1982).
[45] A. J. Lorquet, J. C. Lorquet, J. Delwiche, and M. J. Hubin-Franskin, J. Chem. Phys. **76**, 4692 (1982).
[46] J. E. Pollard, D. J. Trevor, J. E. Reutt, Y. T. Lee, and D. A. Shirley, J. Chem. Phys. **81**, 5302 (1984).
[47] A. B. Myers, R. A. Mathies, D. J. Tannor, and E. J. Heller, J. Chem. Phys. **77**, 3857 (1982).
[48] D. Kosloff and R. Kosloff, J. Comput. Phys. **52**, 35 (1983); R. Kosloff and D. Kosloff, J. Chem. Phys. **79**, 1823 (1983).
[49] This is a result of the properties of a *discrete* Fourier transform (see Ref. 50). The transform is performed between $-t_{max}$ and $+t_{max}$.
[50] W. H. Press, B. P. Flannery, S. A. Teukolsky, and V. T. Vetterling, *Numerical Recipes* (Cambridge University, Cambridge, 1986).
[51] J. M. Bowman, Adv. Chem. Phys. **61**, 115 (1985).
[52] M. E. Jacox, J. Phys. Chem. Ref. Data **13**, 945 (1984).
[53] R. H. Bisseling, R. Kosloff, and J. Manz, J. Chem. Phys. **83**, 993 (1985).
[54] T. N. Kitsopoulos, I. M. Waller, J. G. Loeser, and D. M. Neumark, Chem. Phys. Lett. **159**, 300 (1989).
[55] D. M. Neumark, in Electronic and Atomic Collisions—Invited Papers of the XVI ICPEAC (in press).
[56] I. M. Waller, T. N. Kitsopoulos, and D. M. Neumark, J. Phys. Chem. **94**, 2240 (1990).